Linking the primordial composition of planet building disks to the present-day composition of rocky exoplanets

V. Adibekyan[1,2], M. Deal[3], C. Dorn[4], I. Dittrich[4], B. M. T. B. Soares[1,2], S. G. Sousa[1], N. C. Santos[1,2], B. Bitsch[5], C. Mordasini[6], S. C. C. Barros[1,2], D. Bossini[7,8], T. L. Campante[1,2], E. Delgado Mena[1], O. D. S. Demangeon[1], P. Figueira[9,1], N. Moedas[1,2], Zh. Martirosyan[10], G. Israelian[11,12], and A. A. Hakobyan[13]

[1] Instituto de Astrofísica e Ciências do Espaço, Universidade do Porto, CAUP, Rua das Estrelas, 4150-762 Porto, Portugal
e-mail: vadibekyan@astro.up.pt
[2] Departamento de Física e Astronomia, Faculdade de Ciências, Universidade do Porto, Rua do Campo Alegre, 4169-007 Porto, Portugal
[3] LUPM, Université de Montpellier, CNRS, Place Eugène Bataillon, 34095 Montpellier, France
[4] ETH Zurich, Institute for Particle Physics and Astrophysics, Wolfgang-Pauli-Strasse 27, CH-8093 Zurich Switzerland
[5] Department of Physics, University College Cork, Cork, Ireland
[6] Space Research and Planetary Sciences, Physics Institute, University of Bern, Gesellschaftsstrasse 6, 3012 Bern, Switzerland
[7] Dipartimento di Fisica e Astronomia Galileo Galilei, Università di Padova, Vicolo dell'Osservatorio 3, I-35122 Padova, Italy
[8] Osservatorio Astronomico di Padova – INAF, Vicolo dell'Osservatorio 5, I-35122 Padova, Italy
[9] Observatoire Astronomique de l'Université de Genève, Chemin Pegasi 51b, 1290 Versoix, Switzerland
[10] Department of Astrophysics and General Physics, Yerevan State University, A. Manukyan str. 1, 0025 Yerevan, Armenia
[11] Instituto de Astrofísica de Canarias, E-38205 La Laguna, Tenerife, Spain
[12] Departamento de Astrofisica, Universidad de La Laguna, E-38206 La Laguna, Tenerife, Spain
[13] Center for Cosmology and Astrophysics, Alikhanian National Science Laboratory, 2 Alikhanian Brothers Str., 0036 Yerevan, Armenia

ABSTRACT

Context. The composition of rocky planets is strongly driven by the primordial materials in the protoplanetary disk, which can be inferred from the abundances of the host star. Understanding this compositional link is crucial for characterizing exoplanets.
Aims. We aim to investigate the relationship between the compositions of low-mass planets and their host stars.
Methods. We determined the primordial compositions of host stars using high-precision present-day stellar abundances and stellar evolutionary models. These primordial abundances were then input into a stoichiometric model to estimate the composition of planet-building blocks. Additionally, we employed a three-component planetary interior model (core, mantle, water in different phases) to estimate planetary compositions based only on their radius and mass.
Results. We found that although stellar abundances vary over time, relevant abundance ratios like Fe/Mg remain relatively constant during the main sequence evolution for low temperature stars. A strong correlation is found between the iron-to-silicate mass fraction of protoplanetary disks and planets, while no significant correlation was observed for water mass fractions. The Fe/Mg ratio varies significantly between planets and their stars, indicating substantial disk-driven compositional diversity, and this ratio also correlates with planetary radius.
Conclusions. While stellar abundances, as a proxy of the composition of protoplanetary disk, provide a baseline for planetary composition, significant deviations arise due to complex disk processes, challenging the assumption of a direct, one-to-one elemental relationship between stars and their planets.

Key words. Stars: abundances – Planets and satellites: composition – Planets and satellites: formation

1. Introduction

With the rapid advance in exoplanet science, it is now possible to characterize not only the fundamental parameters (mass and radius) of planets, but also their interior structure and bulk composition (e.g. Dorn et al. 2018; Nettelmann & Valencia 2021; Adibekyan et al. 2021a,b; Armstrong et al. 2020; Helled et al. 2022; Boley et al. 2023). These parameters are important for determining the habitability conditions of terrestrial planets (e.g. Shahar et al. 2019; Unterborn et al. 2022), and understanding the bulk composition is essential for unraveling the origins of planetary diversity (e.g. Owen & Wu 2017; Jin & Mordasini 2018; Bitsch et al. 2019; Venturini et al. 2020).

Information about the mass and radius of exoplanets alone is insufficient to accurately characterize the interior composition of rocky exoplanets (e.g. Valencia et al. 2007; Dorn et al. 2015; Unterborn et al. 2023). To break this degeneracy, the abundances of the main rocky-forming elements (Mg, Si, and Fe) in the host star are often used. Stellar atmospheres offer the only observational window into the remnants of the planet-forming disk's composition, as these disks, with lifetimes typically lasting only a few million years, have long dissipated around most discovered planet-hosting stars.

When modeling the interiors of rocky planets, a one-to-one correlation between the composition of the planet and that of its host star is typically assumed (e.g. Thiabaud et al. 2015; Dorn

et al. 2015; Unterborn et al. 2016). This assumption, to a first-order, appears to be valid for Earth (McDonough 2003), Venus (Aitta 2012), Mars (Khan et al. 2018), and the Sun (see Dorn et al. 2015; Unterborn et al. 2016). It may also be valid for some exoplanets (Santos et al. 2015; Schulze et al. 2021), but not necessarily for others (Bonomo et al. 2019; Plotnykov & Valencia 2020; Brinkman et al. 2023; Mah & Bitsch 2023).

Assuming a one-to-one compositional correlation is a reasonable starting point, but it breaks down even within our own Solar System, in the case of Mercury (Morgan & Anders 1980). Adibekyan et al. (2021a)[1] conducted a statistical comparison of the iron-to-silicate mass fraction in low-mass exoplanets and their host stars, concluding that while there is a correlation between the composition of rocky planets and their host stars, the relationship is not one-to-one. The analysis focused on 22 low-mass ($M < 10\ M_\oplus$) and small-sized ($R < 2\ R_\oplus$) planets with mass and radius measurements precise to within 30%, all orbiting F, G, and K-type stars. However, the study by Adibekyan et al. (2021a) has potential limitations: (i) The planets' interiors were modeled under the assumption that they consist only of a core and mantle, with no volatiles included, and (ii) the present-day stellar abundances were used as a proxy for the primordial protoplanetary disk composition. Some astrophysical processes, such as atomic diffusion, can alter a star's surface composition as it evolves (Deal et al. 2018), meaning that the present-day stellar abundances could differ significantly from their primordial values.

In this work, we study the star-planet compositional link by addressing the aforementioned limitations. Additionally, our sample is approximately 50% larger than that of Adibekyan et al. (2021a) and includes more precise measurements of planetary mass and radius. The paper is structured as follows: In Sect. 2, we introduce the sample. Sect. 3 details the methods used to determine both the primordial composition of the planet-forming disk and the composition of the exoplanets. The star-planet compositional link is discussed in Sect. 4, and we provide a summary of the work in Sect. 5.

2. The sample

We started our sample selection using the PlanetS Catalog (Otegi et al. 2020)[2], which provides a list of transiting exoplanets with relative uncertainties in mass and radius better than 25% and 8%, respectively. Given our focus on potentially rocky planets, we selected only those with radii below $2\ R_\oplus$ to exclude likely gas-rich sub-Neptunes (Fulton et al. 2017; Owen & Wu 2017; Venturini et al. 2020), orbiting F, G, and K-type stars with effective temperatures ($T_{\rm eff}$) ranging between 4600 and 6500 K. This temperature range allows for the precise determination of stellar atmospheric abundances of relevant elements. We excluded Kepler-36 b and Kepler-36 c which have masses determinations via transit timing variation (TTV) method as there might be a discrepancy in the density distributions of planets with mass determinations via TTV and Radial Velocity (RV) method (e.g. Mills & Mazeh 2017; Leleu et al. 2023; Adibekyan et al. 2024). Additionally, we excluded planets orbiting Kepler-65, TOI-1807, TOI-1416, and TOI-1444 due to the unavailability of high-resolution spectra for their host stars. This resulted in a sample of 32 exoplanets orbiting 30 stars, for which we could obtain stellar abundances de-
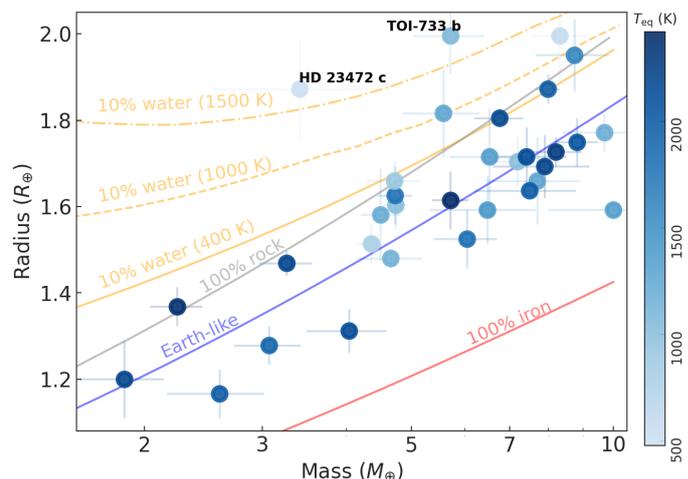
Fig. 1. Distribution of planets in the mass–radius diagram color-coded by their $T_{\rm eq}$. The curves display the expected mass-radius relationship for different compositions taken from Luo et al. (2024).

termined from high-resolution spectra. The distribution of these planets on the Mass-Radius diagram is shown in Figure 1, color-coded by their equilibrium temperatures ($T_{\rm eq}$), as reported in the PlanetS Catalog. The properties of the planets are presented in Table A.1.

3. Present-day and primordial compositions

When conducting stellar spectroscopy, the present-day properties of stars are determined. However, certain properties, including the atmospheric chemical abundances, can change as stars age, even while they remain in the main sequence. In this section, we describe how we determined the primordial compositions of stars hosting planets, and how we used this information to compute the composition of the building blocks of those planets.

3.1. Present-day abundances of the host stars

Given the importance of a consistent characterization of the host stars, we compiled the stellar parameters and chemical abundances of the sample stars from five published articles where these properties were derived using the same methodology and specific tools, making them directly comparable and usable as a single set. This methodology was also applied to K2-131, EPIC 249893012, and HD 20329 in this study. We re-derived the parameters and abundances of EPIC 249893012 and HD 20329 using higher quality spectra obtained with the ESPRESSO spectrograph (Pepe et al. 2021). These parameters and their corresponding references are listed in Table A.2.

In all cases, the stellar atmospheric parameters ($T_{\rm eff}$, surface gravity $\log g$, microturbulent velocity $V_{\rm tur}$, and metallicity [Fe/H]) and the abundances were determined following the methods outlined in our previous works (e.g. Santos et al. 2013; Sousa 2014; Adibekyan et al. 2012, 2015). In our local thermodynamic equilibrium (LTE) analysis, we measured the equivalent widths (EW) of iron lines using the ARES v2 code[3] (Sousa et al. 2015), ensuring excitation and ionization equilibrium. We employed a grid of Kurucz model atmospheres (Kurucz 1993)

---

[1] See also Plotnykov & Valencia (2020); Schulze et al. (2021); Wang et al. (2022); Liu & Ni (2023); Spaargaren et al. (2023); Unterborn et al. (2023); Schulze et al. (2024); Brinkman et al. (2024).
[2] https://dace.unige.ch/

[3] The latest version of the ARES code (ARES v2) can be downloaded at https://github.com/sousasag/ARES

and the 2014 version of the radiative transfer code MOOG (Sneden 1973). The abundances of Mg and Si were derived using the classical curve-of-growth analysis method under the LTE assumption. Although the EWs of the spectral lines were automatically measured with ARES, we visually inspected the EW measurements to ensure accuracy.

Since determining the abundances of C and O is particularly challenging for stars cooler than about 5200 K, we decided to maintain homogeneity by predicting the abundances of these elements using a machine-learning model developed in Adibekyan et al. (2024). This model predicts the abundances of C and O based on the input abundances of Fe, Si, and Mg wth a precision of about 0.07 dex.

3.2. Primordial abundances of the host stars

We used a grid-based modeling approach (similar to Deal et al. 2021) to determine the ages and primordial abundances of the planet hosting stars. The grid of stellar models is computed with the public Code d'Evolution Stellaire Adaptatif et Modulaire[4] (Cesam2k20, Morel & Lebreton 2008; Marques et al. 2013; Deal et al. 2018). The parameter space of the grid varies in mass, primordial iron abundance [Fe/H]$_{prim}$ and helium mass fraction Y_{prim}, and the core overshoot parameter α_{ov}. In terms of chemical transport, the grid includes atomic diffusion with radiative accelerations (Deal et al. 2018), the transport induced by rotation (Marques et al. 2013), and we added an extra turbulent mixing calibrated on the Sun to reproduce its lithium surface abundance. The transport of chemicals is followed for H, He, Li, Be, B, C, N, O, Ne, Na, Mg, Si, Al, S, Ca, Fe, and some of their isotopes. The input physics is the same as the models presented in Deal et al. (2020) for atomic diffusion, rotation and the microphysics, except that the primordial metal mixture follows Asplund et al. (2021), the $T(\tau)$ relation in the atmosphere follows Vernazza et al. (1981), and the convection formalism follows Böhm-Vitense (1958) with a solar-calibrated mixing-length parameter $\alpha_{MLT} = 1.998$.

The stellar property inferences are performed with the Bayesian Asteroseismic Inference on a Massive Scale public code[5] (AIMS, Rendle et al. 2019). The stellar properties are inferred using $\log g$, T_{eff} and [Fe/H] as constraints, in a configuration of the code where no seismic constraints are required. Note that the observed [Fe/H] is directly compared to the one predicted by the models and not to the total metallicity [M/H] for a better accuracy (Deal et al. 2018; Moedas et al. 2022). From the posterior distributions obtained for each star, we derive the fundamental stellar properties (mass, radius, and age) and the primordial chemical composition from each elements followed by the code. The provided error bars are the 16th and 84th percentiles of the distributions.

The ages and primordial abundances of the sample stars are presented in Table A.3.

In Fig. 2, we display the amplitude of the iron abundance change as a function of the age and temperature of the stars. The figure illustrates that the oldest stars experience the most significant reduction in iron abundance and that, for a given age, atomic diffusion is more pronounced in hotter stars due to their narrower convective envelopes. Furthermore, the figure highlights that the temporal change in metallicity can be several times larger than the uncertainties in the present-day [Fe/H] measurements.
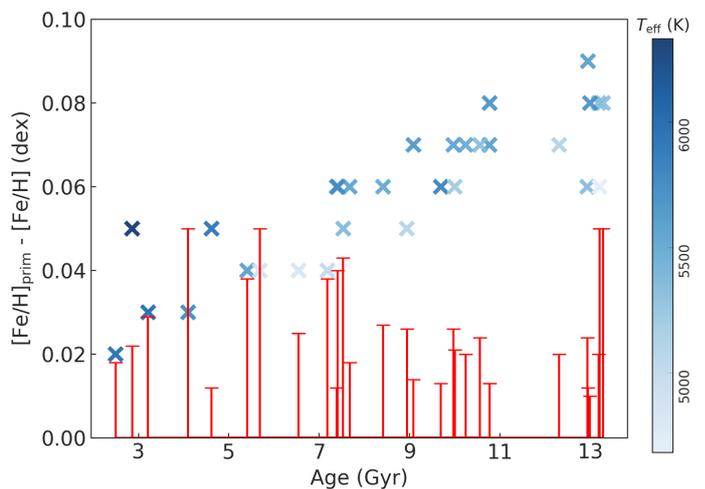
Fig. 2. Difference (crosses) between primordial and present-day abundances of iron as a function of age and color-coded by T_{eff}. The red errorbars represent the uncertainties of present-day [Fe/H].
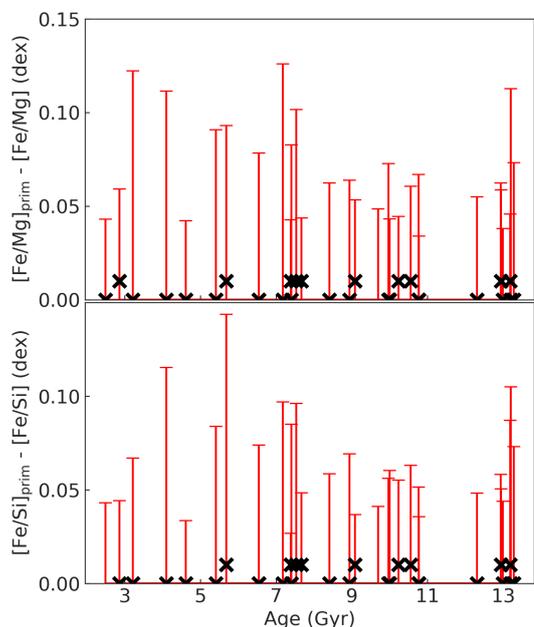

Fig. 3. Difference (crosses) between primordial and present-day abundance ratios of [Fe/Si] and [Fe/Mg] as a function of age. The red errorbars represent the uncertainties of present-day [Fe/Si] and [Fe/Mg].

The overall trend depicted in Fig.2 is consistent when considering other elements used in this work. This consistency is important as it suggests that the changes in abundance ratios remain negligible, as illustrated in Fig.3.

It is important to note that the impact of atomic diffusion generally depends on the competing transport processes included in the models (Moedas et al. 2022). A different treatment of rotation or additional mixing could also influence the results (see e.g. Deal et al. 2020). Furthermore, for hotter stars above ~6500 K, atomic diffusion may cause more pronounced changes in abundance ratios. However, since we have added extra mixing calibrated to reproduce the Sun's lithium abundance, any variations in the efficiency of rotation or diffusion would be compensated by this calibration, resulting in a negligible impact on our results.
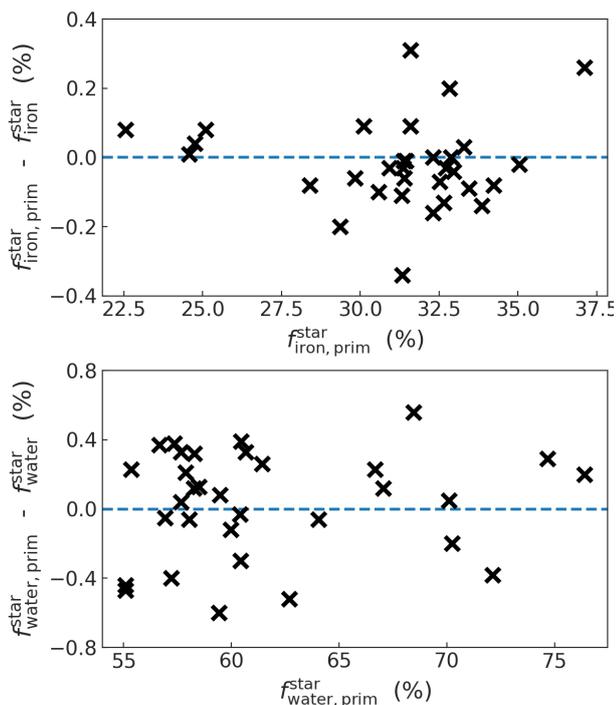
Fig. 4. Difference in iron-to-silicate mass (top) and water mass (bottom) fractions of planet building blocks determined from the present-day and primordial stellar abundances. The differences are plotted as a function of $f_{\mathrm{iron,prim}}^{\mathrm{star}}$ and $f_{\mathrm{water,prim}}^{\mathrm{star}}$, respectively.

3.3. Composition of planet building blocks

We converted the derived primordial atmospheric abundances of C, O, Mg, Si, and Fe into absolute abundances (Adibekyan 2019) using solar reference values from Asplund et al. (2021) and assuming a hydrogen atom number ϵ_H of 10^{12}. These absolute stellar abundances were then used to estimate the iron-to-silicate mass fraction ($f_{\mathrm{iron}}^{\mathrm{star}}$) and the water mass fraction ($f_{\mathrm{water}}^{\mathrm{star}}$) of the protoplanetary disks using the stoichiometric model described in Santos et al. (2015, 2017). Note that $f_{\mathrm{iron}}^{\mathrm{star}}$ does not depend on water availability. For the protosolar disk, the model predicts an $f_{\mathrm{iron}}^{\oplus}$ of 32.3±2.1% and an $f_{\mathrm{water}}^{\oplus}$ of 58.2±3.2% using solar abundances from Asplund et al. (2021).

The present-day and primordial compositions of planet building blocks are displayed in Table A.4.

In Fig.4, we illustrate the impact of using primordial stellar abundances instead of present-day values on $f_{\mathrm{iron}}^{\mathrm{star}}$ and $f_{\mathrm{water}}^{\mathrm{star}}$. The largest difference in the iron-to-silicate mass fraction is approximately 0.4%, with the lowest uncertainty for this parameter around 1% and a mean uncertainty of about 2.2%. A similar trend is observed for the water mass fraction, with the largest difference of about 0.8%, which is approximately 6 times and 8 times smaller than the minimum and mean uncertainty of this parameter, respectively. This behavior is consistent with the results from Sect. 3.2, where we demonstrated that while individual element abundances experience significant temporal changes, their ratios remain relatively stable over time. Consequently, when using Fe/Mg and Fe/Si mineralogical ratios to determine the composition of planet-building blocks, it is generally acceptable to use present-day stellar atmospheric abundances for these low temperature stars.

In Fig. 5, we show how the scaled densities of planets ($\rho/\rho_{\mathrm{Earth-like}}$) depend on the primordial iron-to-silicate mass fraction ($f_{\mathrm{iron,prim}}^{\mathrm{star}}$) and the primordial water mass fraction ($f_{\mathrm{water,prim}}^{\mathrm{star}}$).

The scaled density is calculated by dividing the bulk density (ρ) of the planet by the density of a planet with Earth-like composition ($\rho_{\mathrm{Earth-like}}$, Luo et al. 2024) for the same planetary mass. Throughout this paper, unless stated otherwise, we performed Ordinary Least Squares (OLS) regression using the `statsmodels` package to quantify relationships. The slopes and associated uncertainties were then used in t-statistics (via `SCIPY`) to test the null hypothesis that the data can be modeled with a zero slope. The null hypothesis is rejected if the resulting two-tailed p-values (P(t-stat)) are below the typical threshold of 0.05. We opted for OLS over Orthogonal Distance Regression (ODR), which was used in Adibekyan et al. (2021a), based on the discussion in Brinkman et al. (2024), which concluded that there is a non-negligible probability of obtaining a statistically significant relation when using ODR on a sample similar to ours.

Compared to Adibekyan et al. (2021a), the top panel of Fig. 5 shows two low-density planets (TOI-733 b and HD 23472 c) orbiting stars with solar $f_{\mathrm{iron,prim}}^{\mathrm{star}}$. In Fig. 1, these two planets are the farthest from the Earth-like composition curve, and our interior analysis suggests that they contain a significant amount of water (above 10%, see Table A.5), potentially in the form of steam. We excluded these two planets from the regression analysis shown in Fig. 5. It is important to note that $f_{\mathrm{iron,prim}}^{\mathrm{star}}$ refers to the iron-to-silicate mass ratio and does not account for water in the calculation.

The top panel of Fig. 5 depicts that low-density planets are likely formed in protoplanetary disks with a low iron-to-silicate mass fraction, with an OLS regression p-value of 0.002 suggesting a statistically significant correlation between scaled density and $f_{\mathrm{iron,prim}}^{\mathrm{star}}$. This correlation was previously noted in Adibekyan et al. (2021a). It is important to distinguish that $f_{\mathrm{iron,prim}}^{\mathrm{star}}$ and [Fe/H] of the host stars are different parameters. Furthermore, there is no statistically significant correlation (p-value ~ 0.08) between scaled density and [Fe/H].

The bottom panel of Fig. 5 suggests a possible negative correlation between scaled density and $f_{\mathrm{water,prim}}^{\mathrm{star}}$. However, this trend is not statistically significant, with a p-value of 0.07. Overall, both low iron content and high water content are likely factors contributing to the low density of rocky planets.

Interestingly, the density gap between super-Mercuries and super-Earths appears less pronounced compared to the findings of Adibekyan et al. (2021a), which is in line with the results of some resent studies (Brinkman et al. 2024; Schulze et al. 2024). This discrepancy can be attributed to updated mass and radius determinations and stronger precision constraints on these parameters for the sample planets. Notably, the four highest-density planets in our sample orbit stars with above-average $f_{\mathrm{iron,prim}}^{\mathrm{star}}$.

Additionally, HD 20329 b, which orbits a star with a very low $f_{\mathrm{iron,prim}}^{\mathrm{star}}$, has a scaled density similar to that of Earth. This suggests that HD 20329 b might have a significantly higher $f_{\mathrm{iron}}^{\mathrm{planet}}$ (see. Fig. 6) than what would be expected from its host star's protoplanetary disk composition, potentially classifying it as a super-Mercury (Schulze et al. 2021). Adibekyan et al. (2021a) previously proposed that the formation of high-density super-Mercuries might be linked to the composition of the host star, a hypothesis that has been further explored theoretically in Johansen & Dorn (2022); Mah & Bitsch (2023).
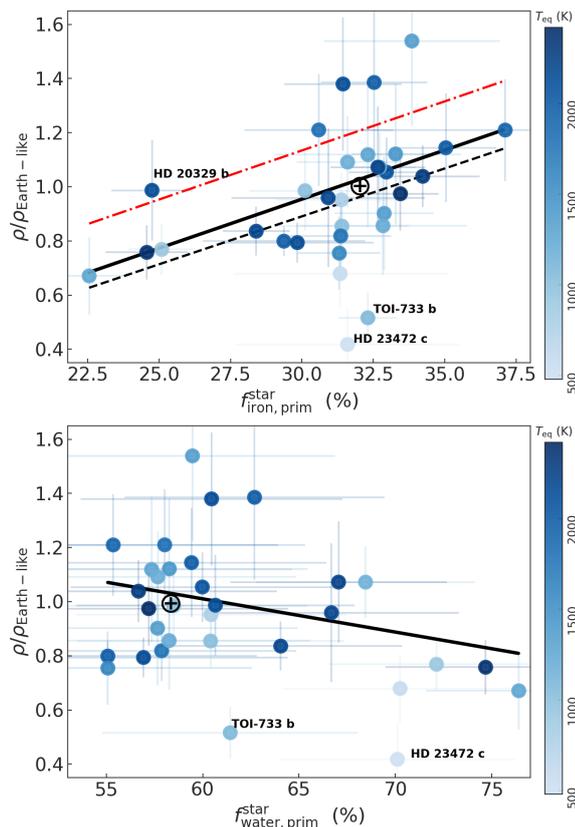
Fig. 5. Scaled density of planets as a function of $f_{\mathrm{iron,prim}}^{\mathrm{star}}$ (top) and $f_{\mathrm{water,prim}}^{\mathrm{star}}$ (bottom) color-coded by the equilibrium temperature of the planets. The positions of Earth is indicated with its symbols in black. The black solid lines represent the results of OLS regression without considering TOI-733 b and HD 23472 c. The red dashed-dotted line represent the visual separation between super-Earths and super-Mercuries. The black dashed line represent the result of the linear regression without considering TOI-733 b, HD 23472 c and the super-Mercuries located above the red line (p-value of about 10^{-5}).

3.4. Interior composition of exoplanets

To compare stellar abundances with planetary abundances, we use inference methods to estimate the confidence regions for the planetary iron-to-silicate mass fraction ($f_{\mathrm{iron}}^{\mathrm{planet}}$), the water mass fraction ($f_{\mathrm{water,prim}}^{\mathrm{star}}$), and the iron-to-magnesium ratio (($Fe/Mg)_{\mathrm{planet}}$).

We use an interior model with 3 components: core, mantle, and water (mainly steam). The model is based on Dorn et al. (2015) with updates from Luo et al. (2024). The water can be present in the core, the mantle, and the surface, depending on the specific thermal state of the planets. In brief, the interior model uses different sets of equation of states for the iron in the core (Hakim et al. 2018; Miozzi et al. 2020; Luo et al. 2024), for silicates in the mantle (Fischer et al. 2011; Faik et al. 2018; Hemley et al. 1992; Musella et al. 2019; Connolly 2009), and surface water (mainly in steam phase for the planets of interest Haldemann et al. 2020). We assume adiabatic temperature profiles in the core, mantle and steam layer, except for pressures below 0.1 bar in the steam layer where we assume an isothermal profile. Additionally, we assumed a pure iron core and fixed the Mg/Si number ratio to 1.04, which is representative of Earth-like composition. The planet radius is set at 1 mbar.

Water can be added to the mantle melts, while the solid mantle is assumed to be dry. The addition of water reduces the den-
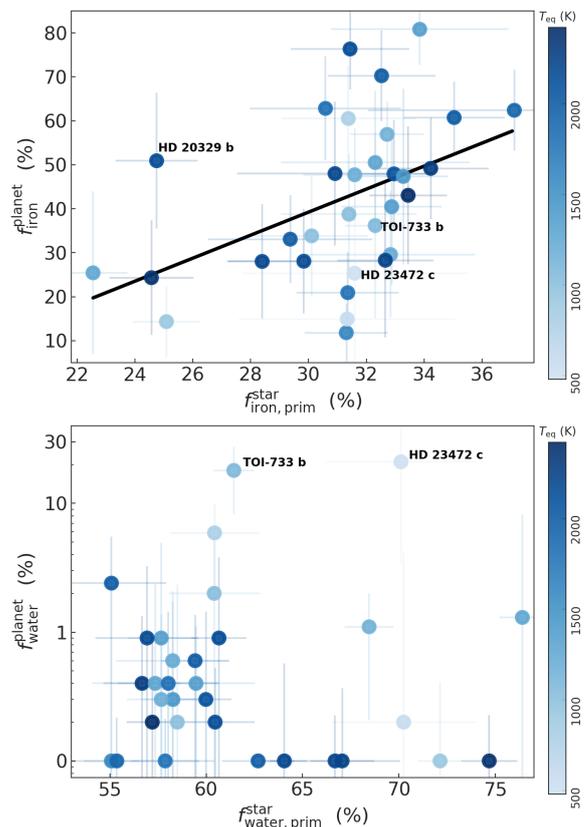
Fig. 6. Iron-to-silicate and water mass fractions of planets and their host stars color-coded by the equilibrium temperature of the planets. The black solid line represents the results of OLS regression.

sity, for which we follow Bajgain et al. (2015). For small water mass fractions, this reduction is nearly independent of pressure and temperature. Further, water can be present in the core for which we use the equation of states of (Luo et al. 2024), that accounts for the reduction in density. Further details on the model can be found in Luo et al. (2024).

The composition of the planets are presented in Table A.5.

4. Star–planet compositional link

Having independently determined the iron-to-silicate mass fractions from both the stellar composition, and the planetary mass and radius, we can now examine the compositional link between solar-type stars and their low-mass planets. The top panel of Fig. 6 shows the relationship between planetary $f_{\mathrm{iron}}^{\mathrm{planet}}$ and stellar $f_{\mathrm{iron,prim}}^{\mathrm{star}}$. The OLS regression analysis, with a slope of 2.6±0.9 and p-value of 0.009, indicates a significant correlation between these two parameters. Given the ongoing discussion in the literature about this relationship, and to ensure the robustness of this result, we applied different regression methods (Appendix B), accounting for the uncertainties in the parameters. While the exact form of the relation varies with the methodology used, the presence of a steeper-than-one-to-one correlation remains evident. The figure also reveals that the range of planetary iron-to-silicate mass fractions is significantly larger than that of the protoplanetary disk, confirming the previous findings (Plotnykov & Valencia 2020; Adibekyan et al. 2021a).

In the bottom panel of Fig. 6, we display the relationship between planetary and protoplanetary water mass fractions. The absence of a clear correlation is somewhat expected, given
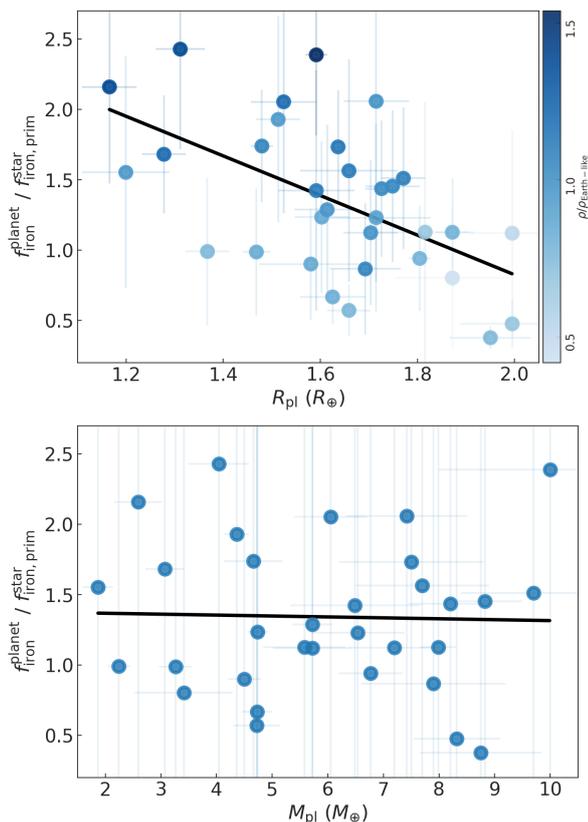
Fig. 7. The ratio of iron-to-silicate mass fraction of planets and the planet building blocks as a function of planetary radius (top panel) and mass (bottom panel). The black solid lines represent the results of the linear regression. The symbols in the top panel are color-coded by the scaled density of the planets.

that $f_{\text{water,prim}}^{\text{star}}$ is calculated with the assumption that the planet-building blocks are located outside the water snowline. The low water content observed in most of the studied planets may actually suggest that they formed inside the water snowline. Several recent studies have also suggested a low water content in close-in super-Earths (Müller et al. 2024; Rogers et al. 2024).

We further explore the planet-star compositional link by examining the ratio of $f_{\text{iron}}^{\text{planet}}$ to $f_{\text{iron,prim}}^{\text{star}}$ as a function of planetary radius (top panel of Fig.7) and planetary mass (bottom panel of Fig.7). There is a clear correlation between this ratio and planetary radius (p-value < 0.001), and no correlation with planetary mass (p-value of about 0.9). This is most likely due to the fact that planetary density depends on radius with a cubic relation, while the dependence on mass is only linear. However, the top panel also shows that for a given radius, denser planets have a higher ratio of $f_{\text{iron}}^{\text{planet}}$ to $f_{\text{iron,prim}}^{\text{star}}$.

As planetary interiors are often modeled under the assumption that the Fe/Mg ratio in planets is similar to that of their host stars, Fig.8 illustrates how the Fe/Mg planet-to-host ratio varies with planetary radius. The figure reveals that the Fe/Mg ratio in planets can be up to three times lower or up to ten times higher than in their host stars, indicating a large variation between the formed planets and the protoplanetary disk. This substantial variation suggests that processes occurring within the protoplanetary disk during planet formation play a significant role in determining the final composition of rocky planets. Additionally, Fig.8 shows a clear dependence of the (Fe/Mg)planet / (Fe/Mg)star ratio on planetary radius.
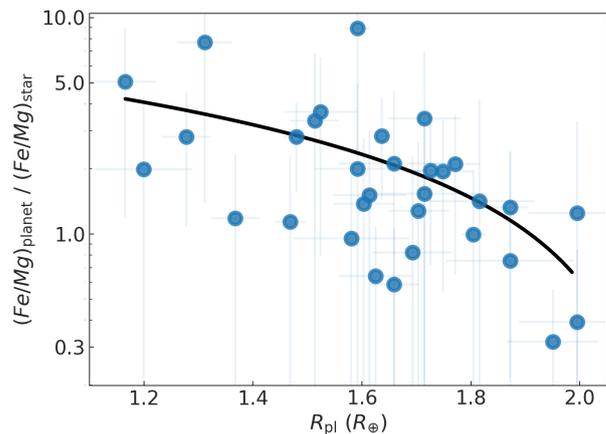
Fig. 8. The Fe/Mg abundance ratio of planets and their host stars as a function of planetary radius. The black solid line in the plot represent the results of the OLS regression (p-value ∼ 0.006) performed on the linearly scaled data.

5. Summary

In this work, we analyzed a sample of 32 low-mass planets orbiting 30 FGK-type stars to investigate the compositional link between stars and their planets. The selected planets from the PlanetS Catalog have relative uncertainties in mass and radius better than 25% and 8%, respectively. Compared to our previous study (Adibekyan et al. 2021a), the current sample includes about 50% more planets, and our analysis was enhanced by determining the primordial compositions of the hosts and using a planetary interior model that accounts also for presence water (primarily in steam form).

We derived the primordial stellar abundances of C, O, Mg, Si, and Fe from their present-day atmospheric values, demonstrating that while individual elemental abundances can vary significantly over time, the ratios between them remain relatively stable. Note that this may not be true for hotter stars, and that the exact values are subject to the assumptions and limitations of the modeling.

We then used the primordial abundances as input for the stoichiometric model presented in Santos et al. (2015) to estimate the iron-mass fraction ($f_{\text{iron,prim}}^{\text{star}}$) and water-mass fraction ($f_{\text{water,prim}}^{\text{star}}$) of the protoplanetary disks. When comparing the present-day and primordial compositions of the planet-building disks, we found negligible differences, as the abundance ratios of Fe/Mg and Fe/Si remain relatively constant over the evolution of stars in the main sequence. This consistency suggests that using present-day stellar abundances to infer the composition of protoplanetary disks is a valid approach, as the key elemental ratios critical for planet formation do not change significantly over time.

Our analysis revealed a strong correlation between the scaled density of rocky planets and the primordial iron-to-silicate mass fraction of their protoplanetary disks ($f_{\text{iron,prim}}^{\text{star}}$). Although the density gap between super-Mercuries and super-Earths is less pronounced than previously observed in Adibekyan et al. (2021a), it remains visible.

We employed a three-component planetary interior model (Dorn et al. 2015; Luo et al. 2024) to derive the compositions of the planets based on their mass and radius. While we found a statistically significant correlation between the iron-to-silicate mass fraction of planets and their host stars, no such correlation was observed for the water mass fraction. This lack of correlation

may be due to the assumption in the stoichiometric model that the building blocks of planets formed outside the water snow-line, while the observed low water content suggests formation inside the snowline.

As already found in Adibekyan et al. (2021a), the range of $f_{\rm iron}^{\rm planet}$ is significantly broader than that of their building blocks. This indicates that while the primordial composition of the protoplanetary disk sets a baseline for planetary composition, various processes during planet formation and evolution can lead to substantial deviations in the iron-to-silicate mass fraction of the resulting planets compared to their original building materials.

Additionally, we compared the Fe/Mg ratios in planets and their host stars, finding a variation from 0.3 to 10 times between the two. This ratio was also found to correlate with planetary radius, further indicating that processes within the protoplanetary disk significantly influence the final composition of rocky planets.

In conclusion, we confirm the previous results (Adibekyan et al. 2021a) suggesting that while a correlation exists between the composition of rocky planets and their host stars, the assumption of a strict one-to-one elemental abundance relationship is not supported by our observations.

References

Adibekyan, V. 2019, Geosciences, 9, 105
Adibekyan, V., Dorn, C., Sousa, S. G., et al. 2021a, Science, 374, 330
Adibekyan, V., Figueira, P., Santos, N. C., et al. 2015, A&A, 583, A94
Adibekyan, V., Santos, N. C., Dorn, C., et al. 2021b, Communications of the Byurakan Astrophysical Observatory, 68, 447
Adibekyan, V., Sousa, S. G., Delgado Mena, E., et al. 2024, A&A, 683, A159
Adibekyan, V. Z., Sousa, S. G., Santos, N. C., et al. 2012, A&A, 545, A32
Aitta, A. 2012, Icarus, 218, 967
Armstrong, D. J., Lopez, T. A., Adibekyan, V., et al. 2020, Nature, 583, 39
Asplund, M., Amarsi, A. M., & Grevesse, N. 2021, A&A, 653, A141
Bajgain, S., Ghosh, D. B., & Karki, B. B. 2015, Nature Communications, 6, 8578
Barros, S. C. C., Demangeon, O. D. S., Alibert, Y., et al. 2022, A&A, 665, A154
Bitsch, B., Raymond, S. N., & Izidoro, A. 2019, A&A, 624, A109
Böhm-Vitense, E. 1958, ZAp, 46, 108
Boley, K. M., Panero, W. R., Unterborn, C. T., et al. 2023, ApJ, 954, 202
Bonomo, A. S., Zeng, L., Damasso, M., et al. 2019, Nature Astronomy, 3, 416
Brinkman, C. L., Polanski, A. S., Huber, D., et al. 2024, AJ, submitted, arXiv:2409.08361
Brinkman, C. L., Weiss, L. M., Dai, F., et al. 2023, AJ, 165, 88
Carpenter, B., Gelman, A., Hoffman, M. D., et al. 2017, Journal of Statistical Software, 76, 1–32
Connolly, J. A. D. 2009, Geochemistry, Geophysics, Geosystems, 10
Damasso, M., Rodrigues, J., Castro-González, A., et al. 2023, A&A, 679, A33
Deal, M., Alecian, G., Lebreton, Y., et al. 2018, A&A, 618, A10
Deal, M., Cunha, M. S., Keszthelyi, Z., Perraut, K., & Holdsworth, D. L. 2021, A&A, 650, A125
Deal, M., Goupil, M. J., Marques, J. P., Reese, D. R., & Lebreton, Y. 2020, A&A, 633, A23

Dorn, C., Khan, A., Heng, K., et al. 2015, A&A, 577, A83
Dorn, C., Mosegaard, K., Grimm, S. L., & Alibert, Y. 2018, ApJ, 865, 20
Faik, S., Tauschwitz, A., & Iosilevskiy, I. 2018, Computer Physics Communications, 227, 117
Fischer, R. A., Campbell, A. J., Shofner, G. A., et al. 2011, Earth and Planetary Science Letters, 304, 496
Fulton, B. J., Petigura, E. A., Howard, A. W., et al. 2017, AJ, 154, 109
Hakim, K., Rivoldini, A., Van Hoolst, T., et al. 2018, Icarus, 313, 61
Haldemann, J., Alibert, Y., Mordasini, C., & Benz, W. 2020, Astronomy & Astrophysics, 643, A105, arXiv:2009.10098 [astro-ph]
Helled, R., Werner, S., Dorn, C., et al. 2022, Experimental Astronomy, 53, 323
Hemley, R. J., Stixrude, L., Fei, Y., & Mao, H. K. 1992, in High-Pressure Research: Application to Earth and Planetary Sciences (American Geophysical Union (AGU)), 183–189, _eprint: https://onlinelibrary.wiley.com/doi/pdf/10.1029/GM067p0183
Hogg, D. W., Bovy, J., & Lang, D. 2010, arXiv e-prints, arXiv:1008.4686
Hunter, J. D. 2007, Computing in Science and Engineering, 9, 90
Jin, S. & Mordasini, C. 2018, ApJ, 853, 163
Johansen, A. & Dorn, C. 2022, A&A, 662, A19
Khan, A., Liebske, C., Rozel, A., et al. 2018, Journal of Geophysical Research (Planets), 123, 575
Kurucz, R. L. 1993, SYNTHE spectrum synthesis programs and line data
Leleu, A., Delisle, J. B., Udry, S., et al. 2023, A&A, 669, A117
Liu, Z. & Ni, D. 2023, A&A, 674, A137
Luo, H., Dorn, C., & Deng, J. 2024, Nature Astronomy [arXiv:2401.16394]
Mah, J. & Bitsch, B. 2023, A&A, 673, A17
Marques, J. P., Goupil, M. J., Lebreton, Y., et al. 2013, A&A, 549, A74
McDonough, W. F. 2003, Treatise on Geochemistry, 2, 568
Mills, S. M. & Mazeh, T. 2017, ApJ, 839, L8
Miozzi, F., Matas, J., Guignot, N., et al. 2020, Minerals, 10, 100
Moedas, N., Deal, M., Bossini, D., & Campilho, B. 2022, A&A, 666, A43
Morel, P. & Lebreton, Y. 2008, Ap&SS, 316, 61
Morgan, J. W. & Anders, E. 1980, Proceedings of the National Academy of Sciences, 77, 6973
Müller, J., Bitsch, B., & Schneider, A. D. 2024, A&A, 688, A139
Musella, R., Mazevet, S., & Guyot, F. 2019, Physical Review B, 99, 064110, publisher: American Physical Society
Nettelmann, N. & Valencia, D. 2021, in ExoFrontiers; Big Questions in Exoplanetary Science, ed. N. Madhusudhan, 16–1
Osborn, A., Armstrong, D. J., Cale, B., et al. 2021, MNRAS, 507, 2782
Otegi, J. F., Bouchy, F., & Helled, R. 2020, A&A, 634, A43
Owen, J. E. & Wu, Y. 2017, ApJ, 847, 29
Pepe, F., Cristiani, S., Rebolo, R., et al. 2021, A&A, 645, A96
Plotnykov, M. & Valencia, D. 2020, MNRAS, 499, 932
Rendle, B. M., Buldgen, G., Miglio, A., et al. 2019, MNRAS, 484, 771
Rogers, J. G., Schlichting, H. E., & Young, E. D. 2024, ApJ, 970, 47
Santos, N. C., Adibekyan, V., Dorn, C., et al. 2017, A&A, 608, A94
Santos, N. C., Adibekyan, V., Mordasini, C., et al. 2015, A&A, 580, L13
Santos, N. C., Sousa, S. G., Mortier, A., et al. 2013, A&A, 556, A150
Schulze, J. G., Wang, J., Johnson, J. A., et al. 2024, Planet. sci. j., 5, 71
Schulze, J. G., Wang, J., Johnson, J. A., et al. 2021, Planet. sci. j., 2, 113
Shahar, A., Driscoll, P., Weinberger, A., & Cody, G. 2019, Science, 364, 434
Skipper Seabold & Josef Perktold. 2010, in Proceedings of the 9th Python in Science Conference, ed. Stéfan van der Walt & Jarrod Millman, 92 – 96
Sneden, C. A. 1973, PhD thesis, THE UNIVERSITY OF TEXAS AT AUSTIN
Sousa, S. G. 2014, in Determination of Atmospheric Parameters of B, 297–310
Sousa, S. G., Santos, N. C., Adibekyan, V., Delgado-Mena, E., & Israelian, G. 2015, A&A, 577, A67
Spaargaren, R. J., Wang, H. S., Mojzsis, S. J., Ballmer, M. D., & Tackley, P. J. 2023, ApJ, 948, 53
Thiabaud, A., Marboeuf, U., Alibert, Y., Leya, I., & Mezger, K. 2015, A&A, 580, A30
Unterborn, C. T., Desch, S. J., Haldemann, J., et al. 2023, ApJ, 944, 42
Unterborn, C. T., Dismukes, E. E., & Panero, W. R. 2016, ApJ, 819, 32
Unterborn, C. T., Foley, B. J., Desch, S. J., et al. 2022, ApJ, 930, L6
Valencia, D., Sasselov, D. D., & O'Connell, R. J. 2007, ApJ, 665, 1413
van der Walt, S., Colbert, S. C., & Varoquaux, G. 2011, Computing in Science and Engineering, 13, 22
Venturini, J., Guilera, O. M., Haldemann, J., Ronco, M. P., & Mordasini, C. 2020, A&A, 643, L1
Vernazza, J. E., Avrett, E. H., & Loeser, R. 1981, ApJS, 45, 635
Virtanen, P., Gommers, R., Oliphant, T. E., et al. 2020, Nature Methods, 17, 261
Wang, H. S., Quanz, S. P., Yong, D., et al. 2022, MNRAS, 513, 5829
Wes McKinney. 2010, in Proceedings of the 9th Python in Science Conference, ed. Stéfan van der Walt & Jarrod Millman, 56 – 61

Appendix A: Tables with compositions of stars and their planets

Appendix B: The star–planet compositional relationship

Fig. B.1. Iron-to-silicate mass fractions of planets and their host stars, with different lines representing the results of the linear fits discussed in the manuscript.

Brinkman et al. (2024) recently suggested that both the slope and the significance of the relationship between the iron mass fraction of stars and their rocky planets depend on the fitting algorithm used. In this section, we apply several algorithms to test the robustness of this relationship.

The OLS regression used in the manuscript does not account for the uncertainties in f_{iron}^{planet} and $f_{iron,prim}^{star}$. To address this, we performed a Monte Carlo (MC) test. Assuming Gaussian distributions for the uncertainties in these parameters, centered on their respective values, we randomly sampled values for f_{iron}^{planet} and $f_{iron,prim}^{star}$ neglecting the cases when the values are negative. After 10000 realizations, we obtained a median slope of 1.65±0.78, with a corresponding p-value (P(t-stat)) of 0.043.

As a second method, we applied the Weighted Least Squares (WLS) regression as implemented in `statsmodels` package, using the inverse square of the uncertainties in f_{iron}^{planet} as weights. This yielded a slope of 3.85±1.10 with a p-value of 0.002. We then repeated the previously described MC test for the WLS case. After 10,000 realizations, we obtained a median slope of 2.43±0.89, with a p-value of 0.01.

For the third method, we used Orthogonal Distance Regression (ODR), implemented in `SCIPY`, which accounts for uncertainties in both parameters during fitting. ODR resulted in a slope of 5.98±1.08, with a p-value of about 10^{-5}. Repeating the MC test for ODR over 10,000 realizations, we obtained a median slope of 5.85±1.07, leading to a p-value of $\sim 10^{-5}$.

Our fourth method was Total Least Squares (TLS), a generalization of ODR that also considers observational errors in both variables. For the log-likelihood calculation, we used `astroML` package which follows the prescription of Hogg et al. (2010), and then used the `scipy.optimize` package to maximize it and find the best-fit parameters. After performing the MC test for the TLS method with 10,000 realizations, we obtained a median slope of 24.9±0.9, with a p-value below 10^{-22}.

Finally, we applied `PyStan`, a Python interface to the Bayesian inference package `Stan` (Carpenter et al. 2017) which allowed us to account for uncertainties in both parameters within a Bayesian framework. We used wide priors for the slope, intercept, and sigma (the scale of the noise term), modeled as normal distributions centered at zero with a standard deviation of 100. From the posterior distributions of the slopes, we obtained a median value of 3.06, with a 95% credible interval of [0.8, 5.0]. Notably, less than 4% of the posterior slopes were smaller than 1.

Overall, these tests demonstrate a statistically significant relationship between f_{iron}^{planet} and $f_{iron,prim}^{star}$, with a slope greater than one. In Fig. B.1 we show the results of the aforementioned linear fits.

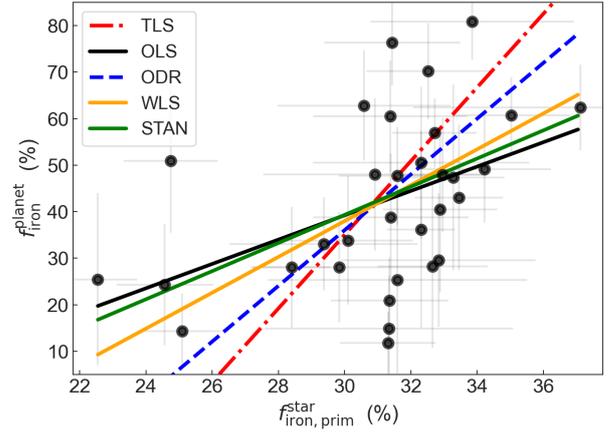**Table A.1.** The main properties of the planets.

Planet	M ($M_\oplus$)	R ($R_\oplus$)	$\rho/\rho_{\mathrm{Earth-like}}$	T_{eq} (K)
55 Cnc e	$7.989^{+0.32}_{-0.33}$	$1.87^{+0.034}_{-0.034}$	0.80±0.05	1986
EPIC 249893012 b	$8.749^{+1.09}_{-1.08}$	$1.95^{+0.090}_{-0.078}$	0.75±0.14	1596
HD 137496 b	$4.039^{+0.55}_{-0.55}$	$1.31^{+0.056}_{-0.045}$	1.38±0.25	2141
HD 213885 b	$8.828^{+0.66}_{-0.65}$	$1.75^{+0.056}_{-0.056}$	1.05±0.13	2083
HD 219134 b	$4.738^{+0.19}_{-0.19}$	$1.60^{+0.056}_{-0.056}$	0.85±0.10	1014
HD 219134 c	$4.360^{+0.22}_{-0.22}$	$1.51^{+0.045}_{-0.045}$	0.95±0.10	782
HD 3167 b	$4.729^{+0.28}_{-0.29}$	$1.63^{+0.078}_{-0.056}$	0.82±0.11	1775
HD 80653 b	$5.720^{+0.36}_{-0.35}$	$1.61^{+0.067}_{-0.067}$	0.97±0.14	2421
EPIC 220674823 b	$8.209^{+0.76}_{-0.74}$	$1.73^{+0.034}_{-0.034}$	1.04±0.11	2290
K2-111 b	$5.581^{+0.74}_{-0.73}$	$1.82^{+0.112}_{-0.090}$	0.67±0.14	1266
K2-229 b	$2.590^{+0.43}_{-0.43}$	$1.17^{+0.067}_{-0.045}$	1.39±0.30	1980
K2-265 b	$6.540^{+0.84}_{-0.84}$	$1.71^{+0.112}_{-0.112}$	0.90±0.21	1362
K2-291 b	$6.489^{+1.16}_{-1.16}$	$1.59^{+0.090}_{-0.067}$	1.12±0.26	1420
K2-38 b	$7.700^{+1.20}_{-1.10}$	$1.66^{+0.101}_{-0.101}$	1.12±0.27	1280
Kepler-10 b	$3.261^{+0.30}_{-0.30}$	$1.47^{+0.034}_{-0.022}$	0.84±0.09	2196
Kepler-107 c	$9.998^{+2.00}_{-2.00}$	$1.59^{+0.022}_{-0.022}$	1.54±0.31	1352
Kepler-20 b	$9.699^{+1.30}_{-1.30}$	$1.77^{+0.056}_{-0.034}$	1.09±0.17	1183
Kepler-78 b	$1.869^{+0.27}_{-0.26}$	$1.20^{+0.090}_{-0.090}$	0.96±0.26	2200
Kepler-93 b	$4.659^{+0.53}_{-0.53}$	$1.48^{+0.022}_{-0.022}$	1.07±0.13	1149
HD 15337 b	$7.198^{+0.81}_{-0.81}$	$1.70^{+0.056}_{-0.056}$	0.99±0.15	1000
TOI-561 b	$2.240^{+0.20}_{-0.20}$	$1.37^{+0.045}_{-0.045}$	0.76±0.10	2373
WASP-47 e	$6.769^{+0.57}_{-0.57}$	$1.80^{+0.022}_{-0.022}$	0.79±0.07	2166
HD 20329 b	$7.421^{+1.09}_{-1.09}$	$1.71^{+0.067}_{-0.067}$	0.99±0.19	2149
Kepler-21 b	$7.500^{+1.30}_{-1.30}$	$1.64^{+0.022}_{-0.011}$	1.14±0.20	1995
CoRoT-7 b	$6.054^{+0.65}_{-0.65}$	$1.52^{+0.067}_{-0.067}$	1.21±0.21	1800
HIP 29442 c	$4.500^{+0.30}_{-0.30}$	$1.58^{+0.101}_{-0.112}$	0.86±0.18	1214
TOI-733 b	$5.720^{+0.70}_{-0.68}$	$2.00^{+0.090}_{-0.090}$	0.52±0.09	1066
TOI-431 b	$3.070^{+0.35}_{-0.35}$	$1.28^{+0.045}_{-0.045}$	1.21±0.19	1898
K2-131 b	$7.901^{+1.30}_{-1.30}$	$1.69^{+0.090}_{-0.056}$	1.07±0.22	2227
HD 23472 b	$8.320^{+0.78}_{-0.79}$	$2.00^{+0.112}_{-0.101}$	0.68±0.13	570
HD 23472 c	$3.410^{+0.88}_{-0.81}$	$1.87^{+0.123}_{-0.112}$	0.42±0.13	479
HD 136352 b	$4.719^{+0.42}_{-0.42}$	$1.66^{+0.045}_{-0.045}$	0.77±0.09	908

Table A.2. The stellar atmospheric parameters and present-day abundances of the planet host stars.

Star	T_{eff} (K)	log g (dex)	V_{tur} (km/s)	[Fe/H] (dex)	[Mg/H] (dex)	[Si/H] (dex)	[C/H] (dex)	[O/H] (dex)	Ref.
55 Cnc	5341±62	4.26±0.14	0.94±0.09	0.32±0.04	0.42±0.06	0.35±0.05	0.28±0.10	0.33±0.10	1
CoRoT-7	5288±27	4.40±0.07	0.90±0.05	0.02±0.02	0.03±0.03	0.07±0.08	-0.01±0.10	0.05±0.10	2
EPIC 220674823	5522±34	4.34±0.05	0.87±0.05	0.10±0.03	0.07±0.05	0.05±0.03	0.00±0.10	0.05±0.10	2
EPIC 249893012	5571±17	4.05±0.03	1.03±0.03	0.19±0.02	0.23±0.05	0.20±0.03	0.11±0.10	0.17±0.10	5
HD 136352	5664±14	4.39±0.02	0.85±0.02	-0.34±0.01	-0.14±0.03	-0.23±0.04	-0.23±0.10	0.01±0.10	2
HD 137496	5799±61	4.05±0.10	1.16±0.02	-0.03±0.04	0.01±0.02	-0.03±0.03	-0.06±0.10	0.02±0.10	2
HD 15337	5081±43	4.21±0.13	0.71±0.10	0.03±0.03	0.09±0.04	0.06±0.05	0.01±0.10	0.07±0.10	2
HD 20329	5573±16	4.29±0.03	0.85±0.03	-0.11±0.02	0.08±0.05	0.03±0.04	0.01±0.10	0.05±0.10	5
HD 213885	5885±15	4.39±0.03	1.06±0.02	0.00±0.01	-0.01±0.04	-0.01±0.03	-0.06±0.10	0.02±0.10	1
HD 219134	4789±54	4.15±0.19	0.69±0.14	-0.03±0.03	-0.03±0.06	0.00±0.06	-0.09±0.10	0.02±0.10	1
HD 23472	4684±99	4.53±0.08	0.25±0.49	-0.20±0.05	-0.19±0.09	-0.18±0.08	-0.25±0.10	0.01±0.10	3
HD 3167	5306±36	4.35±0.07	0.69±0.06	0.04±0.02	0.10±0.04	0.03±0.04	-0.01±0.10	0.05±0.10	1
HD 80653	5942±23	4.34±0.05	1.14±0.03	0.34±0.02	0.31±0.03	0.33±0.03	0.26±0.10	0.32±0.10	2
HIP 29442	5289±35	4.39±0.03	0.74±0.06	0.24±0.05	0.26±0.04	0.21±0.04	0.17±0.10	0.24±0.10	4
K2-111	5775±60	4.25±0.15	1.02±0.50	-0.47±0.01	-0.20±0.04	-0.30±0.03	-0.31±0.10	0.01±0.10	2
K2-131	5090±30	4.39±0.07	0.99±0.06	-0.12±0.02	-0.14±0.04	-0.12±0.03	-0.16±0.10	0.01±0.10	5
K2-229	5196±35	4.39±0.07	0.91±0.06	-0.06±0.02	-0.07±0.03	-0.06±0.05	-0.13±0.10	0.01±0.10	1
K2-265	5466±26	4.36±0.05	0.77±0.05	0.09±0.02	0.11±0.03	0.05±0.04	0.00±0.10	0.07±0.10	1
K2-291	5541±24	4.39±0.06	0.97±0.04	0.09±0.02	0.10±0.03	0.04±0.04	0.00±0.10	0.07±0.10	1
K2-38	5731±66	4.38±0.11	0.98±0.03	0.26±0.05	0.24±0.05	0.27±0.06	0.21±0.10	0.25±0.10	1
Kepler-10	5669±16	4.33±0.03	0.92±0.02	-0.14±0.01	-0.01±0.03	-0.10±0.03	-0.10±0.10	0.01±0.10	1
Kepler-107	5958±37	4.21±0.05	1.25±0.04	0.42±0.03	0.41±0.11	0.37±0.04	0.32±0.10	0.42±0.10	1
Kepler-20	5502±35	4.40±0.06	0.83±0.06	0.05±0.03	0.07±0.04	0.06±0.03	0.00±0.10	0.05±0.10	1
Kepler-21	6331±30	4.20±0.03	1.45±0.03	0.04±0.02	-0.03±0.05	-0.01±0.03	-0.09±0.10	0.03±0.10	2
Kepler-78	4993±72	4.43±0.20	0.97±0.16	-0.14±0.04	-0.15±0.10	-0.09±0.07	-0.16±0.10	0.01±0.10	1
Kepler-93	5620±17	4.41±0.03	0.72±0.03	-0.14±0.01	-0.14±0.04	-0.16±0.02	-0.19±0.10	0.01±0.10	1
TOI-431	4850±75	4.60±0.06	0.80±0.10	0.20±0.05	0.10±0.07	0.11±0.13	0.06±0.10	0.10±0.10	6
TOI-561	5314±20	4.37±0.04	0.54±0.05	-0.39±0.02	-0.18±0.04	-0.27±0.03	-0.28±0.10	0.01±0.10	1
TOI-733	5652±16	4.42±0.04	0.90±0.03	-0.04±0.01	-0.02±0.04	-0.05±0.01	-0.10±0.10	0.01±0.10	2
WASP-47	5559±52	4.32±0.12	1.09±0.07	0.40±0.04	0.46±0.06	0.43±0.05	0.35±0.10	0.42±0.10	1

References. (1) Adibekyan et al. (2021a); (2) Adibekyan et al. (2024); (3) Barros et al. (2022); (4) Damasso et al. (2023); (5) This work; (6) Osborn et al. (2021)

Table A.3. The ages and primordial abundances of the planet host stars.

star	[Fe/H]$_{init}$ (dex)	[Mg/H]$_{init}$ (dex)	[Si/H]$_{init}$ (dex)	[C/H]$_{init}$ (dex)	[O/H]$_{init}$ (dex)	Age (Gyr)
55 Cnc	0.37±0.07	0.46±0.08	0.39±0.07	0.32±0.11	0.37±0.11	$7.53^{+4.31}_{-7.51}$
CoRoT-7	0.10±0.03	0.10±0.04	0.14±0.08	0.06±0.10	0.12±0.10	$13.19^{+0.36}_{-0.41}$
EPIC 220674823	0.17±0.04	0.14±0.06	0.12±0.04	0.07±0.10	0.12±0.10	$9.97^{+1.76}_{-2.51}$
EPIC 249893012	0.26±0.04	0.30±0.06	0.27±0.04	0.18±0.10	0.24±0.10	$10.77^{+1.18}_{-1.28}$
HD 136352	-0.26±0.02	-0.06±0.03	-0.15±0.04	-0.14±0.10	0.09±0.10	$12.99^{+0.41}_{-0.54}$
HD 137496	0.03±0.06	0.07±0.05	0.03±0.06	0.01±0.11	0.08±0.11	$7.41^{+1.55}_{-1.61}$
HD 15337	0.08±0.04	0.14±0.05	0.11±0.06	0.06±0.10	0.12±0.10	$8.94^{+3.88}_{-7.99}$
HD 20329	-0.02±0.03	0.16±0.05	0.11±0.05	0.07±0.10	0.13±0.10	$12.95^{+0.32}_{-0.37}$
HD 213885	0.05±0.02	0.04±0.04	0.04±0.03	-0.01±0.10	0.07±0.10	$4.62^{+1.03}_{-1.09}$
HD 219134	0.01±0.04	0.01±0.07	0.04±0.06	-0.05±0.10	0.06±0.10	$6.54^{+5.73}_{-5.96}$
HD 23472	-0.14±0.06	-0.13±0.10	-0.12±0.09	-0.19±0.11	0.07±0.11	$13.20^{+0.26}_{-0.32}$
HD 3167	0.11±0.04	0.16±0.05	0.09±0.05	0.05±0.10	0.11±0.10	$10.56^{+2.57}_{-8.01}$
HD 80653	0.36±0.03	0.33±0.03	0.36±0.03	0.29±0.10	0.35±0.10	$2.49^{+1.00}_{-1.57}$
HIP 29442	0.32±0.06	0.34±0.05	0.29±0.05	0.25±0.10	0.32±0.10	$13.28^{+0.32}_{-0.36}$
K2-111	-0.41±0.02	-0.13±0.05	-0.23±0.04	-0.24±0.10	0.08±0.10	$9.69^{+3.10}_{-6.81}$
K2-131	-0.05±0.03	-0.07±0.05	-0.05±0.04	-0.09±0.10	0.08±0.10	$12.31^{+0.58}_{-0.63}$
K2-229	0.00±0.03	-0.01±0.03	0.00±0.05	-0.07±0.10	0.07±0.10	$10.00^{+3.02}_{-9.37}$
K2-265	0.16±0.03	0.17±0.03	0.11±0.05	0.07±0.10	0.13±0.10	$10.24^{+2.04}_{-2.94}$
K2-291	0.15±0.03	0.15±0.03	0.09±0.04	0.06±0.10	0.12±0.10	$7.67^{+2.54}_{-3.43}$
K2-38	0.29±0.08	0.27±0.08	0.30±0.08	0.25±0.12	0.28±0.12	$4.10^{+2.20}_{-2.82}$
Kepler-10	-0.06±0.02	0.07±0.03	-0.02±0.03	-0.02±0.10	0.09±0.10	$10.77^{+1.32}_{-1.69}$
Kepler-107	0.45±0.04	0.44±0.11	0.40±0.05	0.35±0.10	0.45±0.10	$3.22^{+0.51}_{-3.19}$
Kepler-20	0.11±0.04	0.13±0.05	0.12±0.04	0.06±0.10	0.11±0.10	$8.41^{+2.78}_{-3.68}$
Kepler-21	0.09±0.03	0.01±0.05	0.04±0.03	-0.04±0.10	0.08±0.10	$2.86^{+0.16}_{-0.15}$
Kepler-78	-0.10±0.06	-0.11±0.11	-0.05±0.08	-0.12±0.11	0.05±0.11	$7.18^{+5.04}_{-5.40}$
Kepler-93	-0.07±0.02	-0.08±0.05	-0.10±0.03	-0.12±0.10	0.07±0.10	$9.09^{+2.02}_{-2.36}$
TOI-431	0.24±0.06	0.13±0.07	0.14±0.13	0.09±0.10	0.13±0.10	$5.68^{+0.95}_{-0.80}$
TOI-561	-0.33±0.04	-0.11±0.05	-0.20±0.04	-0.21±0.10	0.08±0.10	$12.93^{+0.68}_{-2.52}$
TOI-733	0.02±0.02	0.03±0.04	0.00±0.02	-0.04±0.10	0.06±0.10	$7.39^{+0.60}_{-0.53}$
WASP-47	0.44±0.06	0.50±0.07	0.47±0.06	0.39±0.11	0.46±0.11	$5.41^{+2.45}_{-3.45}$

Table A.4. The present-day and primordial compositions of planet building blocks.

star	$f_{\mathrm{iron}}^{\mathrm{star}}$ (%)	$f_{\mathrm{water}}^{\mathrm{star}}$ (%)	$f_{\mathrm{iron,prim}}^{\mathrm{star}}$ (%)	$f_{\mathrm{water,prim}}^{\mathrm{star}}$ (%)
55 Cnc	29.3±2.7	55.6±7.6	29.3±2.7	55.5±8.0
EPIC 249893012	31.4±1.5	55.5±7.5	31.3±1.5	55.1±7.5
HD 137496	31.4±2.1	60.7±6.7	31.5±2.2	60.5±6.9
HD 213885	33.1±1.3	60.4±6.9	32.9±1.3	59.7±6.9
HD 219134	31.4±2.4	60.3±7.2	31.3±2.4	60.2±7.2
HD 3167	31.3±1.8	57.8±7.2	31.4±1.9	57.6±7.2
HD 80653	33.5±1.3	57.9±7.1	33.5±1.4	57.8±7.3
EPIC 220674823	34.3±2.0	56.5±7.4	34.3±2.0	56.0±7.3
K2-111	22.5±1.1	76.6±4.8	22.6±1.1	76.4±4.6
K2-229	32.5±1.8	63.0±6.7	32.5±1.8	62.8±6.5
K2-265	32.8±1.7	57.3±7.1	32.8±1.6	57.6±7.3
K2-291	33.3±1.5	58.2±7.1	33.3±1.5	58.1±6.6
K2-38	32.3±3.2	57.7±7.2	32.4±3.2	57.4±7.6
Kepler-10	28.4±1.2	64.0±6.5	28.4±1.1	64.1±6.6
Kepler-107	33.9±3.2	59.5±7.3	33.8±3.2	59.2±7.4
Kepler-20	31.5±1.8	57.1±7.3	31.5±1.8	57.5±7.2
Kepler-78	30.8±3.4	66.4±6.5	31.0±3.4	66.4±6.5
Kepler-93	32.8±1.3	68.1±5.6	32.8±1.3	68.1±5.7
HD 15337	30.0±2.0	58.6±7.1	30.1±2.1	58.8±7.0
TOI-561	24.5±1.5	74.5±5.0	24.6±1.4	74.4±5.3
WASP-47	29.8±2.7	57.2±7.4	29.9±2.6	56.8±7.8
HD 20329	24.7±1.5	60.6±7.0	24.7±1.5	60.6±7.2
Kepler-21	34.9±1.7	59.7±6.9	35.0±1.7	60.2±7.1
CoRoT-7	30.7±2.5	58.5±7.5	30.5±2.6	57.8±7.7
HIP 29442	32.8±2.8	58.7±7.1	32.8±2.9	58.5±7.0
TOI-733	32.3±1.0	61.4±6.6	32.3±1.0	61.0±6.8
TOI-431	37.1±4.9	55.3±8.4	36.8±5.2	55.1±8.4
K2-131	32.6±1.6	66.6±6.1	32.8±1.6	67.3±6.2
HD 23472	31.3±3.9	70.2±6.1	31.7±3.8	70.4±6.2
HD 136352	25.0±1.1	72.4±5.3	25.1±1.1	72.6±5.4

Table A.5. The compositions of planets.

Planet	f_{mantle} (%)	f_{Fe} (%)	f_{water} (%)	$f_{\mathrm{iron}}^{\mathrm{planet}}$	(Fe/Mg)$_{\mathrm{planet}}$
55 Cnc e	$65.4^{+11.1}_{-20.8}$	$32.3^{+16.2}_{-9.8}$	$2.3^{+4.7}_{-1.6}$	$33.1^{+10.3}_{-9.7}$	$0.9^{+1.1}_{-0.4}$
EPIC 249893012 b	$88.2^{+7.8}_{-7.5}$	$11.8^{+7.5}_{-7.8}$	$0.0^{+0.0}_{-0.0}$	$11.1^{+6.5}_{-6.8}$	$0.2^{+0.2}_{-0.2}$
HD 137496 b	$23.6^{+12.2}_{-11.0}$	$76.1^{+11.0}_{-11.9}$	$0.1^{+0.6}_{-0.1}$	$77.0^{+9.0}_{-9.5}$	$5.7^{+6.6}_{-2.5}$
HD 213885 b	$51.8^{+17.7}_{-16.5}$	$47.7^{+14.7}_{-17.3}$	$0.2^{+2.2}_{-0.1}$	$47.6^{+12.6}_{-11.9}$	$1.6^{+1.5}_{-0.9}$
HD 219134 b	$59.9^{+14.8}_{-23.8}$	$37.9^{+19.2}_{-13.7}$	$1.9^{+5.7}_{-1.4}$	$38.6^{+13.9}_{-13.6}$	$1.1^{+1.7}_{-0.6}$
HD 219134 c	$37.1^{+16.6}_{-19.0}$	$56.8^{+15.2}_{-13.8}$	$5.8^{+4.6}_{-3.3}$	$62.1^{+11.4}_{-12.4}$	$2.7^{+4.3}_{-1.3}$
HD 3167 b	$79.1^{+10.9}_{-11.2}$	$20.9^{+11.1}_{-10.9}$	$0.0^{+0.2}_{-0.0}$	$19.7^{+8.9}_{-9.4}$	$0.5^{+0.4}_{-0.3}$
HD 80653 b	$56.6^{+20.6}_{-21.5}$	$42.8^{+20.6}_{-20.1}$	$0.1^{+1.3}_{-0.1}$	$42.2^{+16.1}_{-15.2}$	$1.3^{+1.9}_{-0.8}$
EPIC 220674823 b	$50.6^{+17.3}_{-13.7}$	$49.0^{+12.3}_{-16.9}$	$0.3^{+1.5}_{-0.3}$	$49.5^{+11.6}_{-11.6}$	$1.7^{+1.2}_{-0.9}$
K2-111 b	$73.0^{+18.7}_{-37.6}$	$24.9^{+26.4}_{-17.2}$	$1.2^{+12.5}_{-1.2}$	$23.4^{+19.6}_{-17.4}$	$0.6^{+1.9}_{-0.5}$
K2-229 b	$29.7^{+16.1}_{-12.4}$	$70.2^{+12.4}_{-16.1}$	$0.0^{+0.0}_{-0.0}$	$70.4^{+10.2}_{-19.5}$	$4.2^{+4.3}_{-2.1}$
K2-265 b	$58.2^{+21.7}_{-22.8}$	$39.6^{+22.9}_{-20.0}$	$0.8^{+7.3}_{-0.8}$	$41.0^{+17.7}_{-17.9}$	$1.2^{+2.3}_{-0.8}$
K2-291 b	$52.2^{+27.3}_{-26.8}$	$46.9^{+24.9}_{-26.4}$	$0.2^{+2.7}_{-0.2}$	$46.7^{+19.6}_{-20.3}$	$1.6^{+3.5}_{-1.1}$
K2-38 b	$48.9^{+23.7}_{-23.1}$	$49.9^{+20.2}_{-22.6}$	$0.3^{+3.7}_{-0.2}$	$51.7^{+16.1}_{-16.6}$	$1.8^{+2.9}_{-1.1}$
Kepler-10 b	$71.9^{+13.1}_{-21.6}$	$28.0^{+20.7}_{-13.0}$	$0.0^{+0.9}_{-0.0}$	$25.0^{+15.1}_{-10.8}$	$0.7^{+1.0}_{-0.4}$
Kepler-107 c	$19.0^{+12.1}_{-7.9}$	$79.9^{+8.0}_{-11.7}$	$0.3^{+1.2}_{-0.2}$	$81.4^{+8.3}_{-8.0}$	$7.5^{+6.6}_{-3.5}$
Kepler-20 b	$52.0^{+15.1}_{-16.2}$	$47.5^{+14.5}_{-14.9}$	$0.2^{+2.0}_{-0.1}$	$47.2^{+10.5}_{-19.6}$	$1.6^{+1.4}_{-0.8}$
Kepler-78 b	$52.0^{+22.5}_{-22.8}$	$48.0^{+22.6}_{-22.4}$	$0.0^{+0.2}_{-0.0}$	$47.4^{+17.4}_{-15.4}$	$1.6^{+2.7}_{-1.0}$
Kepler-93 b	$42.6^{+10.6}_{-9.8}$	$56.3^{+9.1}_{-10.2}$	$1.0^{+1.2}_{-0.6}$	$57.5^{+7.5}_{-7.5}$	$2.3^{+1.2}_{-0.8}$
HD 15337 b	$65.6^{+15.2}_{-24.1}$	$33.6^{+21.9}_{-14.4}$	$0.1^{+4.2}_{-0.1}$	$32.6^{+14.8}_{-12.8}$	$0.9^{+1.4}_{-0.5}$
TOI-561 b	$75.7^{+13.6}_{-18.4}$	$24.3^{+18.1}_{-13.5}$	$0.0^{+0.2}_{-0.0}$	$22.6^{+13.3}_{-12.8}$	$0.6^{+0.7}_{-0.4}$
WASP-47 e	$71.3^{+10.8}_{-22.7}$	$27.8^{+18.8}_{-10.3}$	$0.8^{+4.0}_{-0.7}$	$27.8^{+12.3}_{-11.4}$	$0.7^{+1.0}_{-0.3}$
HD 20329 b	$48.5^{+21.5}_{-22.2}$	$50.4^{+17.7}_{-20.9}$	$0.8^{+5.1}_{-0.7}$	$51.9^{+14.6}_{-16.2}$	$1.8^{+2.7}_{-1.1}$
Kepler-21 b	$38.9^{+12.1}_{-10.0}$	$60.2^{+9.7}_{-11.6}$	$0.5^{+1.2}_{-0.4}$	$60.0^{+8.2}_{-8.1}$	$2.7^{+1.5}_{-1.0}$
CoRoT-7 b	$36.8^{+16.9}_{-14.8}$	$62.2^{+14.2}_{-16.3}$	$0.3^{+1.8}_{-0.2}$	$63.3^{+11.5}_{-12.1}$	$3.0^{+3.2}_{-1.5}$
HIP 29442 c	$69.8^{+15.3}_{-24.3}$	$29.3^{+22.3}_{-14.7}$	$0.5^{+2.4}_{-0.5}$	$27.4^{+15.6}_{-13.1}$	$0.7^{+1.3}_{-0.4}$
TOI-733 b	$52.0^{+29.5}_{-27.1}$	$29.5^{+20.4}_{-18.8}$	$17.9^{+8.9}_{-10.6}$	$29.1^{+28.1}_{-14.2}$	$1.0^{+2.5}_{-0.8}$
TOI-431 b	$37.6^{+13.0}_{-11.9}$	$62.3^{+11.8}_{-13.0}$	$0.0^{+0.2}_{-0.0}$	$63.0^{+9.5}_{-9.0}$	$2.9^{+2.2}_{-1.2}$
K2-131 b	$71.7^{+12.2}_{-33.2}$	$28.3^{+32.1}_{-12.2}$	$0.0^{+0.5}_{-0.0}$	$22.0^{+22.8}_{-12.3}$	$0.7^{+2.1}_{-0.4}$
HD 23472 b	$83.7^{+10.8}_{-19.7}$	$14.7^{+14.8}_{-9.8}$	$0.1^{+7.9}_{-0.1}$	$14.1^{+11.6}_{-11.1}$	$0.3^{+0.5}_{-0.2}$
HD 23472 c	$61.2^{+26.3}_{-35.0}$	$20.8^{+20.0}_{-14.9}$	$20.9^{+14.4}_{-20.8}$	$28.9^{+18.5}_{-21.8}$	$0.6^{+2.1}_{-0.5}$
HD 136352 b	$85.5^{+9.0}_{-10.6}$	$14.3^{+10.4}_{-8.8}$	$0.0^{+0.6}_{-0.0}$	$14.0^{+8.1}_{-8.1}$	$0.3^{+0.3}_{-0.2}$

Notes. f_{mantle}, f_{Fe} (%), and f_{water} are the mantle, iron, and water mass fractions. $f_{\mathrm{iron}}^{\mathrm{planet}}$ is the ratio of f_{Fe} / (f_{Fe} + f_{mantle}).